Front. Energy 2018, 12(1): 5–21
https://doi.org/10.1007/s11708-017-0517-z

REVIEW ARTICLE

Eric TERVO, Elham BAGHERISERESHKI, Zhuomin ZHANG

Near-field radiative thermoelectric energy converters: a review

Abstract Radiative thermoelectric energy converters, which include thermophotovoltaic cells, thermoradiative cells, electroluminescent refrigerators, and negative electroluminescent refrigerators, are semiconductor p-n devices that either generate electricity or extract heat from a cold body while exchanging thermal radiation with their surroundings. If this exchange occurs at micro or nanoscale distances, power densities can be greatly enhanced and near-field radiation effects may improve performance. This review covers the fundamentals of near-field thermal radiation, photon entropy, and nonequilibrium effects in semiconductor diodes that underpin device operation. The development and state of the art of these near-field converters are discussed in detail, and remaining challenges and opportunities for progress are identified.

Keywords energy conversion systems, luminescent refrigeration, near-field radiation, thermophotovoltaic, thermoradiative cell

1 Introduction

Whenever heat moves from a hot region to a cold region, useful work may be extracted from this process by some type of heat engine. Conversely, work may be supplied to a heat pump to reverse the heat flow from the cold region to the hot one. Heat engines and heat pumps for electricity production and refrigeration usually rely on circulating a working fluid through turbomachinery, heat exchangers, and other flow components. However, with advances in semiconductor technology, there has been a growing interest in alternative solid-state systems that offer the advantages of no moving parts, comparatively simple components, and very compact devices. In particular, semiconductor p-n diodes that interact with either the hot or cold region via thermal radiation are promising candidates for solid-state heat engines and heat pumps (e.g. Refs. [1,2]). In this review, we will refer to these types of devices as radiative thermoelectric energy converters (RTECs). Photovoltaic (PV) cells are the archetypical example of RTECs; they absorb thermal radiation from the sun, which generates electron-hole pairs used to drive current through a load, and they reject heat to the surroundings [3]. For the more general case where any hot object is used as the source of thermal radiation for the photovoltaic cell, the RTEC is called a thermophotovoltaic (TPV) cell [4,5] and is shown in Fig. 1(a).

In addition to operating as a heat engine in a TPV configuration, a semiconductor p-n diode may also be operated as a heat engine or heat pump in three other arrangements. While a cold TPV cell receives thermal radiation from a hot source, a hot p-n diode may instead emit to a colder environment and generate electrical power [6]. This RTEC is termed a thermoradiative (TR) cell and is shown in Fig. 1(b). A TR cell operates like a PV or TPV cell in reverse: current flows across the load from the n-type contact to the p-type contact, and the cell is under a reverse bias instead of the forward bias associated with a PV or TPV cell. As a heat pump, a p-n diode supplied with electrical power is driven out of equilibrium by the external voltage, which causes it to emit either a greater or fewer number of photons than the same material under equilibrium conditions. In the forward bias case, photon emission increases and the RTEC can cool below the temperature of the surroundings [7], which is referred to as electroluminescent (EL) refrigeration and is shown in Fig. 1(c). Under a reverse bias, photon emission decreases, allowing the diode to absorb more net radiation and cool the object radiating to it [8]. This case is called negative electroluminescent (NEL) refrigeration and is shown in Fig. 1(d). While there have been extensive research and development efforts for TPV cells, the other three types of

Received Jun. 13, 2017; accepted Sep. 20, 2017; online Dec. 5, 2017

Eric TERVO, Elham BAGHERISERESHKI, Zhuomin ZHANG (✉)
George W. Woodruff School of Mechanical Engineering, Georgia Institute of Technology, Atlanta, GA 30332, USA
E-mail: zhuomin.zhang@me.gatech.edu

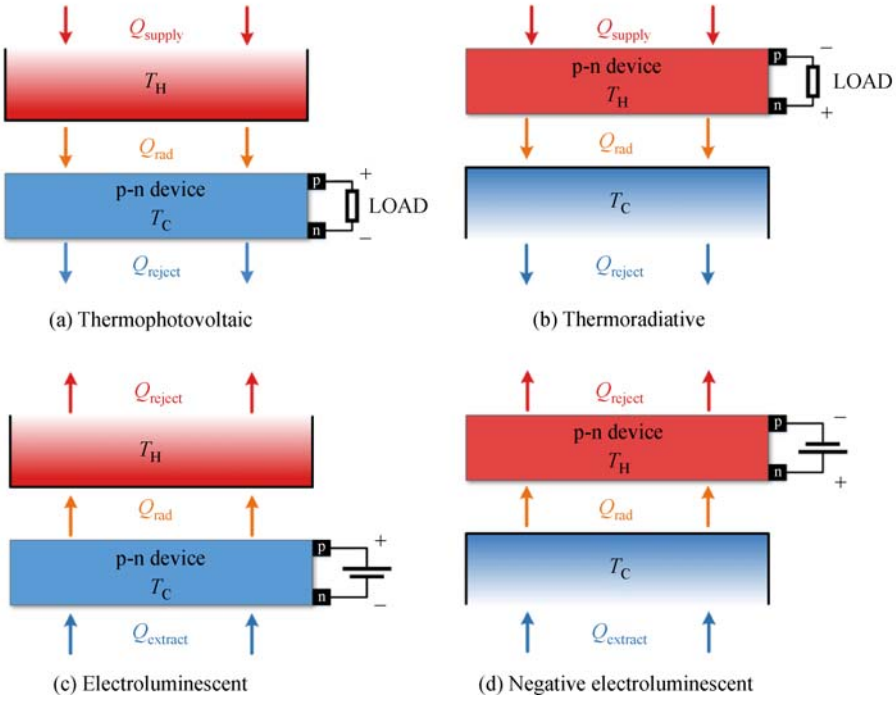

Fig. 1 Schematics of the four types of radiative thermoelectric energy converters (RTECs)
(a) A thermophotovoltaic (TPV) cell absorbs radiation from a heat source and develops a forward bias across the semiconductor p-n diode as it produces electricity; (b) a thermoradiative (TR) cell emits to a colder environment and develops a reverse bias as it produces electricity; (c) an electroluminescent (EL) refrigerator supplied with electricity under a forward bias cools the diode by emitting thermal radiation to a hotter environment; (d) a negative electroluminescent (NEL) refrigerator cools another object by receiving net thermal radiation when it is supplied with electricity under a reverse bias

RTECs (TR, EL, and NEL) have not been as thoroughly studied due to relatively low conversion rates.

When operated with a macroscale distance between the surfaces exchanging thermal radiation, RTEC power densities are restricted by Planck's spectral distribution of blackbody radiation [9]. If the surfaces are brought to separation distances on the order of the characteristic thermal wavelength, however, the radiative heat flux can exceed the blackbody limit [10–24].This heat flux enhancement can be by orders of magnitude if the separation distance is further decreased and the materials are carefully chosen. When the two bodies support surface modes such as surface phonon polaritons or surface plasmon polaritons, the near-field heat flux can also be quasi-monochromatic [25], which may be favorable for RTEC performance. These characteristics, along with significant experimental progress in measuring near-field radiation over the last decade, have motivated researchers to explore how RTECs may be improved by operating in the near-field.

In this article, we provide an overview and background on RTECs with emphasis on the effects of utilizing near-field radiation. We begin with some background information of near-field thermal radiation and then discuss the physics of radiation exchange in biased p-n junctions that underpins RTEC operation. The basics of photon entropy are outlined, which serves to elucidate the device performance and operating limits. These devices are then examined in more detail, beginning with a review of the functional mechanisms of the RTECs. This review focuses on how near-field radiation may improve RTEC performance and highlights the recent research progress for each device. Finally, because many of the same principles and methodologies are used for all of these RTECs, some common lessons are observed and future research opportunities are summarized.

2 Theoretical background

All objects emit thermal radiation due to random thermal fluctuations of charges within the material. At distances from an object greater than the characteristic thermal wavelength $\lambda_T = \hbar\omega/k_B T$, where $\hbar$ is the reduced Planck constant, ω is the angular frequency, k_B is Boltzmann's constant, and T is the temperature, the spectral intensity of thermal emission is given by [9,26]:

$$I(\omega,T) = \frac{\hbar\omega^3}{4\pi^2 c^2} f_{BE}(\omega,T), \tag{1}$$

where $f_{BE}(\omega,T) = [e^{\hbar\omega/(k_B T)} - 1]^{-1}$ is the Bose-Einstein distribution of carriers and c is the speed of light. In this

case, the maximum radiative heat flux between two objects is governed by the Stefan-Boltzmann law as $\sigma(T_1^4 - T_2^4)$, where σ is the Stefan-Boltzmann constant. This classical description must be modified, though, when the distance from the surface is very small and when the chemical potential of photon emission is modified. In addition to the radiation energy exchange in the far- and near-fields, it is instructive to examine the entropy of thermal radiation to gain insight into device operating limits. The following sections provide the fundamental background on these topics.

2.1 Near-field thermal radiation

When the distance between two objects is on the order of λ_T or smaller, the energy transfer can be significantly increased and exceed the far-field blackbody limit [10–19]. This enhancement of near-field radiation transfer is caused by photon tunneling due to the presence of evanescent waves between the objects. When electromagnetic waves travel from a medium 1 to an optically rarer medium 2 at incidence angles greater than the critical angle, the wave is totally reflected inside the first medium as shown in Fig. 2. If total internal reflection occurs, an evanescent wave whose magnitude decays exponentially away from the interface exists in the second medium. The time-averaged Poynting vector normal to the interface is zero, hence energy is not transferred from medium 1 to medium 2. However, if another optically denser medium 3 is placed close to the first medium, a reflected evanescent wave is formed due to the second interface [11]. The Poynting vector of the coupled evanescent fields has a nonzero normal component, and energy is then transmitted between the first and third medium through the second medium as shown in Fig. 2. This phenomenon is known as photon tunneling or radiation tunneling, and this type of evanescent wave is referred to as a frustrated mode. Some materials such as polar dielectrics or noble metals can support evanescent surface modes on both sides of an interface called surface phonon polaritons or surface plasmon polaritons. These are referred to as surface modes and can increase the radiation exchange even further [17].

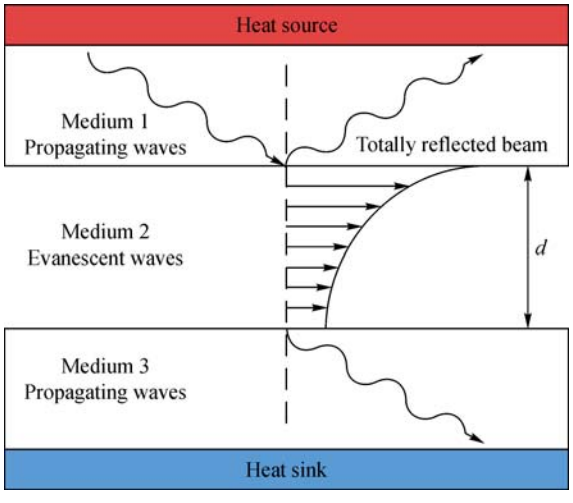

Fig. 2 Schematic of photon tunneling enabling high near-field radiation heat transfer between a hot and cold object. Upon total internal reflection of a propagating electromagnetic wave in medium 1, an exponentially decaying field exists in medium 2. If a third material is brought within micro- or nano-scale distances d from the first material, coupling of the evanescent waves between these objects enables photon tunneling across the gap. The Poynting vector in the gap then has a nonzero normal component, indicating energy transfer between the hot and cold object

Rytov et al. [27] established the theory of fluctuational electrodynamics to analyze these effects by combining Maxwell's equations and the fluctuation-dissipation theorem. According to the fluctuation-dissipation theorem, the random thermal motion of charges in a medium at thermal equilibrium creates the fluctuating currents that lead to thermal emission. The correlation function of these current densities for a non-magnetic medium is given by [12,19]:

$$\langle J_j(\boldsymbol{r},\omega) J_k^*(\boldsymbol{r}',\omega')\rangle = \frac{4\omega\varepsilon_0\Theta(\omega,T)\varepsilon''_{jk}(\boldsymbol{r},\omega)}{\pi}\delta(\boldsymbol{r}-\boldsymbol{r}')\delta(\omega-\omega'), \quad (2)$$

where $\langle\ \rangle$ and * respectively represent the ensemble average and the complex conjugate, j or k denotes a vector component, ε_0 is the vacuum permittivity, and ε''_{jk} is the imaginary part of the dielectric tensor. $\delta(\boldsymbol{r}-\boldsymbol{r}')$ and $\delta(\omega-\omega')$ are the Dirac delta functions representing spatial and temporal incoherence, respectively [14]. The mean energy of a Planck oscillator is $\Theta(\omega,T) = \hbar\omega f_{\mathrm{BE}}(\omega,T)$. Along with the fluctuating currents, dyadic electric and magnetic Green's functions $G^{\mathrm{E}}(\boldsymbol{r},\boldsymbol{r}',\omega)$ and $G^{\mathrm{H}}(\boldsymbol{r},\boldsymbol{r}',\omega)$ can be used to express the induced electric and magnetic fields at a position $\boldsymbol{r}$ related to the source current at $\boldsymbol{r}'$ by:

$$\mathbf{E}(\boldsymbol{r},\omega) = i\omega\mu_0\int_{V'} G^{\mathrm{E}}(\boldsymbol{r},\boldsymbol{r}',\omega)\cdot J(\boldsymbol{r}',\omega)\mathrm{d}V', \quad (3)$$

$$\mathbf{H}(\boldsymbol{r},\omega) = \int_{V'} G^{\mathrm{E}}(\boldsymbol{r},\boldsymbol{r}',\omega)\cdot J(\boldsymbol{r}',\omega)\mathrm{d}V', \quad (4)$$

where μ_0 is the vacuum magnetic permeability, V' is the fluctuating source region, and $i = \sqrt{-1}$. The near-field radiative heat flux between two media (i.e. the emitter and the receiver) is given by the ensemble-averaged Poynting vector as:

$$q'' = \int_0^\infty \frac{1}{2}\langle \mathrm{Re}[\boldsymbol{E}(\boldsymbol{r},\omega)\times\boldsymbol{H}^*(\boldsymbol{r},\omega)]\rangle \mathrm{d}\omega. \quad (5)$$

Combining these equations, the radiative heat flux from medium 1 to medium 3 can be written as:

$$q''_{1\to 3} = \int_0^\infty \frac{2k_0^2}{\pi} \int_{V'} \Theta(\omega, T_1 \boldsymbol{r}') \operatorname{Re}\left[i \sum_{j,k=x,y,z} \varepsilon''_{jk}(\omega) \left(G^{\mathrm{E}}_{xj} G^{\mathrm{H}^*}_{yk} - G^{\mathrm{E}}_{yj} G^{\mathrm{H}^*}_{xk} \right) \right] \mathrm{d}V' \, \mathrm{d}\omega, \quad (6)$$

where $k_0 = \omega/c_0$ is the wave vector in a vacuum. The electric and magnetic dyadic Green's functions can be obtained analytically using the transfer matrix method [18,28,29]. With these equations for multilayer or stratified media, it is possible to find the energy transfer between arbitrary materials, even at micro or nanoscale separation distances.

While near-field radiation heat transfer enhancement has been predicted theoretically for different conditions in many studies, experimental investigations have been relatively limited due to difficulties in maintaining a nanoscale vacuum gap between parallel surfaces. There has been more success in measuring heat transfer between nanostructures such as a probe tip and a surface, and several researchers have done so in the past few years for separation distances down to a few nanometers [24,30–32]. Despite the challenges for larger areas, notable progress has been made for parallel-plate configurations with lateral dimensions up to 1 cm at a few hundred nanometers separation gap. Ijiro et al. [33] measured near-field radiative heat flux between two 25 mm diameter SiO_2 plates with gaps as small as 1 μm, and they reported heat transfers exceeding the blackbody limit for gaps less than 2 μm. Ito et al. [34] measured near-field heat flux between two 8.6 mm × 19 mm fused quartz substrates at gap distances down to 500 nm. Lim et al. [35] devised a MEMS-based platform for doped silicon plates with areas of 6.4 mm^2 and measured radiative heat transfer coefficients of almost three times the blackbody limit at a separation spacing of 400 nm. More recently, Bernardi et al. [36] measured a radiative heat transfer enhancement of 8.4 relative to the blackbody limit for parallel 5 mm by 5 mm intrinsic silicon surfaces at a 150 nm thick vacuum gap, and Watjen et al. [37] reported heat transfers up to 11 times the far-field limit for 1 cm by 1 cm doped-Si plates at separation gaps from 200 nm to 780 nm. Since practical near-field RTECs will require nanoscale gaps over large areas for useful operation, this recent progress is encouraging and should help pave the way for device realization.

2.2 Chemical potential of radiation

The previous equations given for thermal radiation, including the Bose-Einstein statistics used to describe photon populations, are generally only valid for thermal equilibrium. Under equilibrium conditions, the photon distribution emitted carries no chemical potential and is only a function of temperature. However, since photon emission depends directly on photon interaction with electrons, phonons, and other quasiparticles, modification of these quasiparticle states can also modify the photon distribution [38]. For the semiconductor devices of interest, electrical injection and/or radiative nonequilibrium modifies the carrier populations in the valence and conduction bands. This in turn affects the electron-hole recombination rate, which changes the distribution of photon emission (giving the emitted photons a chemical potential) [39]. The photon chemical potential μ is related to the electron and hole chemical potentials by $\mu = \mu_e - \mu_h$ or equivalently to the electron and hole quasi-Fermi levels by $\mu = E_{f,e} - E_{f,h}$. For a semiconductor p-n junction, this chemical potential in the depletion region is also given by $\mu = qV$ where q is the electron charge and V is the bias voltage [3]. The quasi-Fermi levels are used to describe the nonequilibrium populations of electrons and holes in the conduction and valence bands, respectively, in a manner similar to the Fermi level under equilibrium conditions. Even when the p-n junction as a whole is out of equilibrium, the carriers in the conduction and valence bands may separately be in equilibrium with themselves due to the much faster relaxation times for intra-band transitions than for inter-band transitions. This allows the definition of separate electron and hole quasi-Fermi levels [40]. It is important to note that the photon chemical potential is only well-defined once the electron and hole populations in the conduction and valence bands have reached a well-established quasi-equilibrium under steady-state or slowly varying conditions.

A semiconductor emitter with different electron and hole chemical potentials (quasi-Fermi levels) then emits according to the modified Bose-Einstein distribution [39,41]

$$f'_{\mathrm{BE}}(\omega, T, \mu) = \begin{cases} \dfrac{1}{\mathrm{e}^{(\hbar\omega - \mu)/(k_{\mathrm{B}}T)} - 1}, & \hbar\omega \geqslant E_{\mathrm{g}}, \\ \dfrac{1}{\mathrm{e}^{\hbar\omega/(k_{\mathrm{B}}T)} - 1}, & \hbar\omega < E_{\mathrm{g}}, \end{cases} \quad (7)$$

where E_g is the bandgap energy. This leads to a modified form of Planck's law with different spectral intensities above and below the bandgap:

$$I'(\omega, T, \mu) = \frac{\hbar\omega^3}{4\pi^2 c^2} f'_{\mathrm{BE}}(\omega, T, \mu) \quad (8)$$

The spectral intensity is shown in Fig. 3(a) for a semiconductor emitter with a bandgap of 0.2 eV at a temperature of 300 K for different photon chemical potentials (different bias voltages). Below the bandgap, the chemical potential has no effect on the photon emission, but above it the spectral intensity is raised or lowered depending on whether μ is positive or negative (corresponding to the direction of the bias voltage). This demonstrates that a p-n device under a bias voltage may have stronger or weaker photon emission than a device under equilibrium conditions at the same temperature,

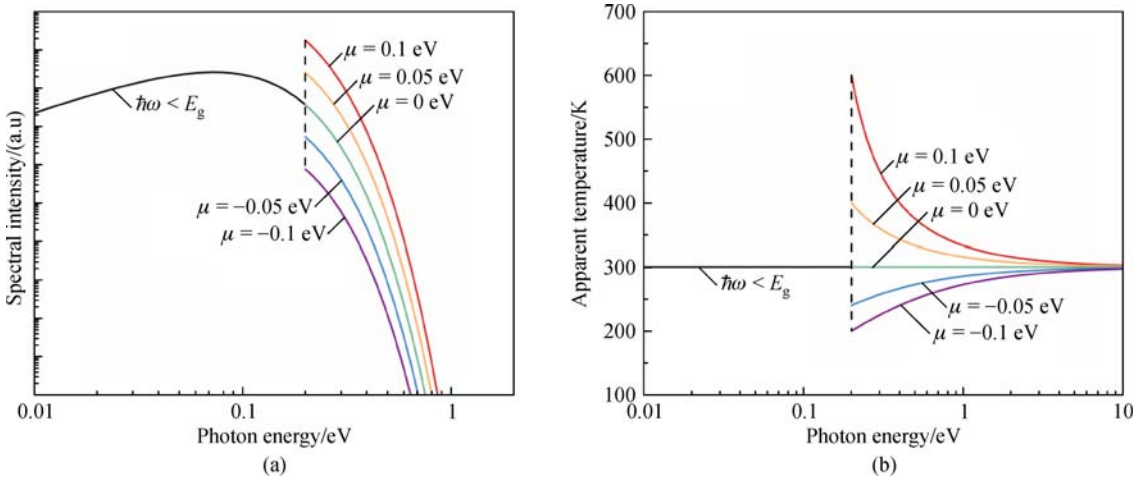

Fig. 3 (a) Spectral intensity and (b) apparent temperature for a semiconductor with a bandgap energy of E_g= 0.2 eV at a temperature of 300 K under varying chemical potential μ. Above the bandgap a positive chemical potential, which corresponds to a forward bias of a p-n junction, is associated with greater photon emission, and the semiconductor therefore appears "hotter" in this spectral region. A negative chemical potential, corresponding to a reverse bias of a p-n junction, reduces photon emission and makes the material appear "colder."

which underlies the operating mechanisms of the EL and NEL RTECs.

Another way to consider the modified photon emission is to define an apparent spectral temperature $T_{\lambda,\mu}$ with the following relation:

$$\frac{\hbar\omega}{k_B T_{\lambda,\mu}} = \frac{\hbar\omega - \mu}{k_B T}. \tag{9}$$

This is plotted in Fig. 3(b) for a bandgap energy of 0.2 eV, temperature of 300 K, and different photon chemical potentials (different bias voltages). Under a positive chemical potential (forward bias) the semiconductor emits more photons above the bandgap, so it appears "hotter" or has a higher apparent temperature. Conversely, under a negative chemical potential (reverse bias) it emits less photons and so appears "colder" with a lower apparent temperature. The concept of apparent temperature helps to illustrate the direction of spectral energy transfer between two surfaces when one or both emits with a photon chemical potential.

2.3 Entropy of thermal radiation

In addition to understanding and predicting the energy flows in a RTEC, it is instructive to examine the entropy transfers. These can give insight into the losses in a particular device, help to determine performance improvements, and establish the limiting efficiencies for the different RTECs. For photons, the statistical entropy of a mode is [9,39,42,43]

$$s_\omega(\omega,T,\mu) = k_B[(1+f'_{BE})\ln(1+f'_{BE}) - f'_{BE}\ln f'_{BE}], \tag{10}$$

where f'_{BE} is Bose-Einstein distribution modified by the chemical potential of radiation as discussed in Section 2.2. The total entropy of a photon flux can then be found by integrating over all frequencies and is

$$s(T,\mu) = k_B \int_0^\infty s_\omega(\omega,T,\mu) D(\omega) \mathrm{d}\omega, \tag{11}$$

where $D(\omega)$ is the density of states. For a blackbody with $\mu = 0$, $D(\omega) = \omega^2/(\pi^2 c^3)$, and the integral becomes $s_{BB}(T) = (4/3)\sigma T^3$.

When compared to the entropy carried by heat conduction $s_{cond}(T) = q''/T$, it is clear that the same heat flux from a blackbody radiation source has a higher entropy content. In other words, the ratio of the entropy flux to energy flux for radiation is $(4/3)\sigma T^3/(\sigma T^4) = (4/3)T^{-1}$ while for conduction it is $(q''/T)/q'' = T^{-1}$. This is better understood by defining a non-dimensional entropy content function $\psi(\omega,T,\mu)$ as

$$\psi(\omega,T,\mu) = \frac{T s_\omega(\omega,T,\mu)}{\Theta'(\omega,T,\mu)}, \tag{12}$$

where $\Theta'(\omega,T,\mu) = \hbar\omega f'_{BE}(\omega,T,\mu)$ is the mean energy of a harmonic oscillator modified by the photon chemical potential. This function is plotted in Fig. 4 for a bandgap energy of 0.2 eV, temperature of 300 K, and various chemical potentials. By examining the case where $\mu = 0$, we see that the blackbody radiation does indeed have a higher entropy content over the whole photon energy spectrum. Low frequency radiation, however, has much higher entropy content than high frequency radiation, which approaches the same value as that for conduction. This is an important characteristic for design of RTECs; for example, if the device must reject heat to the surroundings through radiation exchange, it is much better to do so with

low-frequency radiation, because more entropy can be rejected per photon. Furthermore, we see that a bias voltage modifies the entropy content via the chemical potential. A positive chemical potential (positive bias and higher apparent temperature) leads to radiation with entropy content lower than that of conduction, while a negative chemical potential leads to the opposite. This explains why devices such as lasers with very high intensities at high frequencies have a small entropy flux [44].

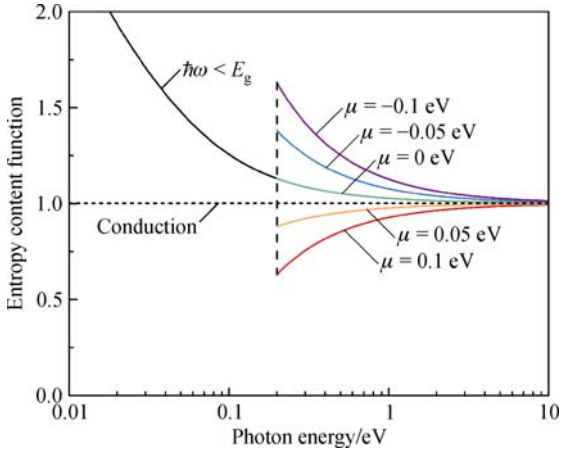

Fig. 4 Entropy content of thermal radiation (solid lines) compared to that of conduction (horizontal dashed line). Blackbody radiation has a higher entropy content than conduction, as evidenced by the higher values over the whole photon energy spectrum. Low-frequency radiation, however, has much higher entropy content than high frequency radiation. This can also be modified by introducing a chemical potential, which can lower the entropy content below that of conduction if $\mu > 0$

For near-field operation of RTECs, the density of states term in Eq. (11) can be enhanced significantly. This means that, along with methods for spectral control of near-field thermal radiation, RTECs can be designed to emit or absorb quasi-monochromatic radiation with a high or low entropy content, depending on the application. An understanding of photon entropy is, therefore, essential to identifying opportunities for device improvement.

3 Radiative thermoelectric energy converters

We now turn our attention to the RTECs themselves. TPV, TR, EL, and NEL devices have received drastically different levels of attention in the literature. For instance, TPV cells began to be researched in the mid-1950s and have since been the subject of thousands of publications [5,13,38,45–48]. In contrast, TR cells have only been proposed and analyzed as recently as 2015 [6]. In the following sections, an overview of the principles of operation of the RTECs is provided, and we then provide some history and review the recent near-field progress for each device.

3.1 Operating principles and performance metrics

The operating principles of each type of device are best understood by examining the corresponding band diagram, shown in Fig. 5. For each diagram, the p-doped semiconductor is on the left and the n-doped is on the right. The valence (E_v) and conduction (E_c) bands are shown by the bottom and top solid black lines. An intrinsic region could be placed between the p-type and n-type materials, forming a p-i-n junction, but the underlying principles are the same. As discussed in Section 2.2, the electron and hole quasi-Fermi levels (dashed blue and red lines) split due to illumination or external bias, endowing the emitted photons with a chemical potential.

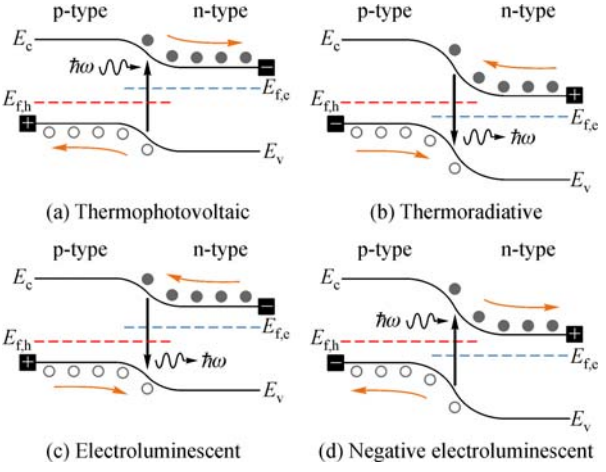

Fig. 5 Band diagrams for radiative thermoelectric energy converters (RTECs) including (a) thermophotovoltaic (TPV) cell, (b) thermoradiative (TR) cell, (c) electroluminescent (EL) refrigerator, and (d) negative electroluminescent (NEL) refrigerator. For each device, the split between the electron and hole quasi-Fermi levels $E_{f,e}$–$E_{f,h}$ corresponds to the bias voltage multiplied by the charge of an electron, qV. Electron-hole pairs are generated (destroyed) by net photon absorption (emission) with energy $\hbar\omega$ above the bandgap for TPV and NEL (TR and EL) devices. The corresponding electron and hole flows are shown along the valence and conduction bands E_v and E_c

In a TPV cell, shown in Fig. 5(a), a heat source radiates photons with energy $\hbar\omega$ above the bandgap to the cell. Absorption of these photons creates electron-hole pairs that are separated by the field at the p-n junction. The electrons and holes drive a current through an external load from the p-type contact to the n-type (current is in the direction of hole flow), which corresponds to a forward bias across the RTEC. The positive forward bias with a negative current driven by external illumination means that the device operates in the fourth quadrant of the current-

voltage diagram, as shown in Fig. 6. Due to the forward bias, photons emitted from the TPV cell have a positive chemical potential, and the device thus appears "hotter" than it is, which can reduce performance. However, in most TPV systems the emitter is at very high temperatures, in which case the effect of chemical potential is negligibly small and often omitted.

For a hot TR cell, shown in Fig. 5(b), the net emission of photons to a colder environment can be thought of as a type of "negative" illumination. This splits the quasi-Fermi levels in the opposite direction from a TPV cell and results in a reverse bias. As the electrons and holes move through the circuit, their energy must also be raised by thermal intra-band transitions in order to overcome the field at the p-n junction. The external heat supply drives this process, which maintains the reverse bias and steady flow of electrons and holes. The resulting current, which flows in the reverse direction compared to a TPV cell, may be provided to an electrical load. TR cells operate in the second quadrant of the current-voltage diagram (see Fig. 6) due to the reverse bias and positive current. The irradiation chemical potential is negative, which reduces photon emission from the cells. Because the temperature gradients considered are usually much smaller than for TPV systems, the effect of chemical potential must be taken into account for these devices.

If an external forward bias voltage is provided to the cell, the device can operate as an EL refrigerator. Electrons (holes) are injected into the conduction (valence) band, splitting the quasi-Fermi levels and resulting in a positive chemical potential as shown in Fig. 5(c). The device thus emits more photons than it would at equilibrium, and some of this photon energy is derived from the thermal energy of the lattice (similar to TR cells). At a sufficiently high operating voltage, the energy of emitted photons exceeds the energy provided by the external supply. The temperature of the EL refrigerator falls below the temperature of its surroundings as a result, and it can then sustain a cooling load. A forward bias and positive current means that the device operates in the first quadrant of the current-voltage diagram, as shown in Fig. 6.

Finally, an external reverse bias supplied to a p-n junction allows it to function as a NEL refrigerator. In this case, the power supply draws electrons (holes) out of the conduction (valence) band, which reduces photon emission and splits the quasi-Fermi levels as shown in Fig. 5(d). Reduced emission means that the net radiation absorption from the exchanging object is higher, which allows that object to cool below ambient temperature. A NEL refrigerator operates with a reverse bias and negative current, so it lies in the third quadrant of the current-voltage diagram shown in Fig. 6.

The performance of all these RTECs is primarily evaluated on the basis of two metrics: efficiency and power density. The limiting efficiency of these devices is the Carnot efficiency, which is the same as that for any heat engine or heat pump. This is given as $1-T_C/T_H$ for a heat engine and $T_C/(T_H-T_C)$ for a refrigerator, where T_H is the hot reservoir temperature and T_C is the cold reservoir temperature. As with any device, though, operating at the Carnot limit would require no entropy generation in the device and is not practically achievable. The power density is the metric for which near-field thermal radiation provides significant improvements. If a RTEC is operating through far-field radiation, its power density is limited by the Stefan-Boltzmann law and must be less than $\sigma(T_H^4-T_C^4)$, as described in Section 2. Near-field radiation enables the devices to exceed this limit and greatly enhance the power density.

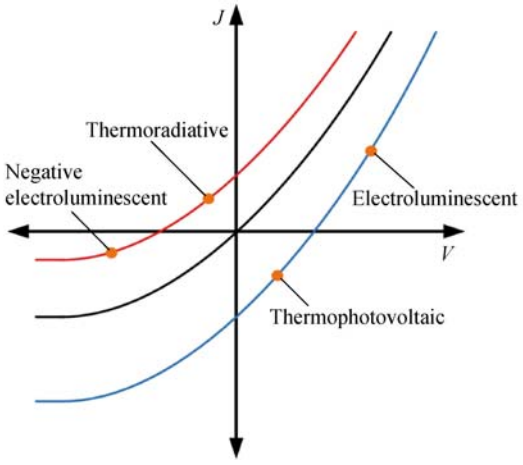

Fig. 6 Plot of current density (J) versus bias voltage (V) for each radiative thermoelectric energy converter. The case of thermal equilibrium is shown by the black curve through the origin. If the diode is exposed to a warmer environment and receives net radiation, the curve shifts down and may operate as a thermophotovoltaic device. Applying a high enough voltage in this condition changes the direction of net thermal radiation to operate as an electroluminescent refrigerator. If the diode is exposed to a colder environment and emits net radiation, the curve shifts up and may operate as a thermoradiative device. Similarly, applying sufficient voltage will change the radiative heat flow direction and become a negative electroluminescent refrigerator

3.2 Thermophotovoltaic cells

Because the source of radiation for PV cells (the sun) is replaced by a terrestrial radiation source for TPV cells, the latter may take advantage of a wide range of heat sources including solar energy collection [48], combustion [49], nuclear reactions (primarily radioisotope) [50], and waste heat recovery [51]. This makes TPV cells promising for many applications such as spacecraft power, remote power generation, and residential cogeneration, to name a few [52].Their development has also been greatly assisted by parallel progress in traditional PV devices due to their similarities in operation. Of the four RTECs, TPV cells

have therefore been by far the most heavily investigated in both far-field and near-field operation. A short history of the early far-field devices from the first demonstration in 1956 to uptake by commercial enterprises in the late 1990s is given by Robert [45], and a detailed discussion on the technology is given in Bauer's book [5]. Far-field TPV devices have made enormous progress, with experimental heat-to-electricity conversion efficiencies as high as about 25% and power densities greater than 300 mW/cm^2 reported [1]. However, their power densities are blackbody-limited, which restricts their effectiveness for widespread use. Most of the recent research in far-field TPV devices focuses on solar-TPV systems [48] (for which solar-to-electricity conversion efficiencies greater than 6% have been reported [53,54]) and optimization of spectral emission/absorption in the TPV system, usually taking advantage of micro- or nano-structured materials [38,47,55–58]. Additional details on far-field TPV RTECs can be found in the aforementioned references.

The application of near-field thermal radiation to TPV devices was first proposed by Whale and Cravalho in 1997 [59,60] and has since been researched analytically [57,61–79] and experimentally [80–82] by many groups. Whale and Cravalho studied how radiation tunneling at microscale gaps, discussed in Section 2.1, could increase the radiative energy transfer from the emitter to the TPV cell and thus increase the output power. Using a fluctuational electrodynamics approach, they showed that the output power density could be increased by an order of magnitude with little impact on the conversion efficiency. This preliminary work analyzed an Indium Gallium Arsenide receiver with a fictitious low-conductivity Drude emitter designed to act like a blackbody, and its power density improvement was primarily a result of additional radiation heat transfer through frustrated modes [59,60]. It was soon realized, though, that choosing emitters and/or receivers that support evanescent surface modes can open additional channels for heat transfer at quasi-monochromatic frequencies, which is beneficial if these are just above the bandgap energy of the TPV cell. Narayanaswamy and Chen [62] theoretically demonstrated this in 2003 by analyzing cubic Boron Nitride, which supports surface phonon polaritons, emitting to a low bandgap PV material. This resulted in very large power absorption in the PV material just above the bandgap energy.

Despite the promise illustrated in early works [59–62], realistic near-field TPV systems must account for many additional factors that degrade performance. These include photocurrent generation [63], spatial distribution of radiation absorption in the TPV cell [64], temperature-dependent electrical and optical properties [65], sub-bandgap parasitic radiation [71], surface and bulk carrier recombination [64,65,72], and thermalization of photon energy greater than the bandgap [65,72]. In particular, the radiative, electrical, and thermal losses can significantly diminish power density. Bernardi et al. [72] analyzed these in detail for both a broadband Tungsten and a narrowband optimized Drude radiator at 2000 K emitting to an $In_{0.18}Ga_{0.82}Sb$ cell cooled by convection for various vacuum gap thicknesses. When all losses are considered, their interplay becomes complex as illustrated in Fig. 7(a), which shows the loss mechanisms for photons of energy E with respect to the bandgap energy E_g. Absorption of photons with $E < E_g$ produces an undesirable heat load on the TPV device. Electron-hole pairs generated by absorption with $E = E_g$ may recombine radiatively, in which their energy is lost through photon emission, or they may recombine non-radiatively and generate heat through Auger, Shockley-Read-Hall, or surface recombination. Thermalization of photons with $E > E_g$ also generates heat. These thermal losses provide feedback (represented by the bi-directional arrows) to make some loss mechanisms even stronger. The importance of capturing all losses is demonstrated in Bernardi et al.'s iterative model which accounts for heat generation and temperature-dependent properties, and the resulting impacts on device performance are shown in Fig. 7(b) [72]. Interestingly, the performance and strength of different loss types vary significantly depending on whether the emitter is broadband Tungsten or narrowband Drude. The Tungsten emitter is dominated by frustrated modes, which penetrate into the cell to a depth on the order of the wavelength. Because of its broadband nature, a significant amount of energy is above the bandgap and is thermalized. The quasi-monochromatic surface modes from the Drude emitter, on the other hand, only penetrate into the TPV cell to a depth on the order of the vacuum gap. This means that surface recombination plays a major role in the losses, because most of the energy is absorbed at or near the surface. As a result, emitters utilizing surface modes may not necessarily outperform broadband emitters when all losses are considered, even at very small separation distances [72]. Additional research is needed to determine whether this conclusion holds for other p-n junction materials and geometries, as well as for different emitter types and materials.

A major research thrust in the theoretical investigation of near-field TPV systems is the design of novel emitting and absorbing systems in order to optimize their radiative exchange. This has included the use of backside mirrors on the cell [70], graphene layer(s) on the front of the cell [67,74,77], hyperbolic metamaterial emitters [68,75,76], thin film emitters and absorbers [57], and emitters with grating structures [79]. The general goal of all of these methods is to maximize the radiation exchange for energies just above the bandgap to increase photocurrent generation and minimize it elsewhere to reduce losses.

Use of a backside mirror accomplishes this by reflecting sub-bandgap radiation back to the emitter instead of allowing it to be absorbed by the substrate and generate

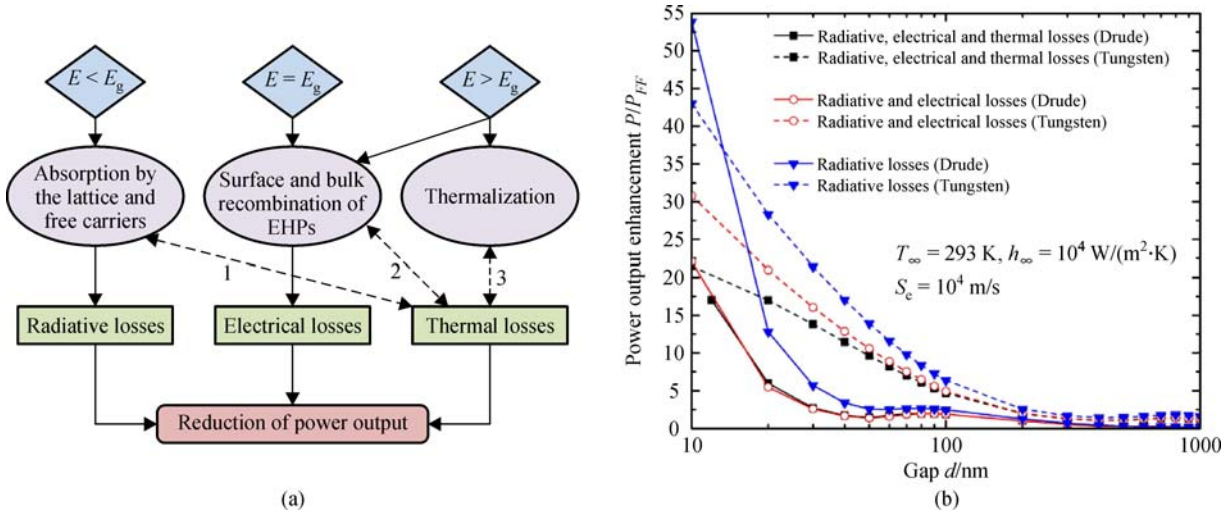

Fig. 7 (a) Interplay of loss mechanisms in TPV devices and (b) effect of different loss types on near-field power enhancement over the far-field value P_{FF} for broadband Tungsten and narrowband optimized Drude emitters. The combination of radiative, electrical, and thermal losses can significantly degrade performance, and these also include feedback mechanisms that further reduce power output. In (b), the TPV cell is cooled by convection with the free-stream temperature and convection coefficient shown in the graph, and it is modeled with a surface recombination velocity S_e as indicated. The Drude emitter only outperforms the Tungsten emitter at very small gap distances when electrical and thermal losses are not considered. (Reprinted figure from Bernardi et al. [72], under Creative Commons CC-BY license.)

heat. For a Tungsten emitter about 1000 K hotter than an InGaSb TPV cell at a 100 nm separation gap, the efficiency can be enhanced up to 35% with a backside mirror compared to a semi-infinite TPV cell [70]. The mirror may also serve as an electrical contact to collect charge carriers. This type of architecture is expected to be particularly useful for TPV systems with thin cells and broadband emitters such as Tungsten, where frustrated modes may penetrate the cell to depths of microns and sub-bandgap exchange can be significant.

Improvements to the absorber in the TPV system include layering graphene on the front and reducing its thickness. If the emitter supports surface plasmons or surface phonon polaritons, the addition of graphene to the absorber creates additional surface modes that couple to those from the emitter. This increases the energy transfer around the emitter's resonant frequency, shifts the spectral radiation towards the bandgap, and can improve both efficiency and power density of the device [67,74]. Adding multiple layers of graphene has the additional benefit of enhancing power output at larger separation distances [77]. Reducing the absorber thickness improves performance in a different way. By shrinking the quasi-neutral p and n regions of the cell until they are negligibly thin compared to the depletion region, bulk recombination will decrease significantly because excited carriers will be immediately separated by the junction field [57].

Improvements to the emitter include using a thin film, hyperbolic metamaterial, or grating structure. Structuring the emitter as a thin film causes it to support trapped waveguide modes that totally reflect back and forth within the film. This leads to high near-field emission due to the frustrated evanescent waves associated with the internal reflection. Additionally, the waveguide dispersion characteristics introduce a cut-off frequency that reduces undesired radiative exchange far above the bandgap [57]. Hyperbolic metamaterial emitters [83,84] may consist of layered materials [68,76] or nanowires immersed in another medium [75]. The anisotropy and restriction of charge motion in one or two directions cause the parallel and perpendicular components of the permittivity to be of opposite sign, which leads to hyperbolic isofrequency surfaces in wave vector space, and very large numbers of modes can participate in near-field thermal radiation. When the geometry of the metamaterial is carefully engineered, the dielectric tensor of the emitter can be altered to optimize the radiative exchange between the emitter and cell. Introducing a grating on the surface of the emitter is another method to tailor the near-field thermal emission. An appropriately designed grating structure can alter the energy transmission coefficient to favor radiative exchange close to the bandgap, which improves device performance [79].

Although near-field TPV systems have received much attention and been modeled by many researchers, there has been comparatively little experimental progress in the field. The first demonstration of near-field effects in a TPV device was in 2001 by DiMatteo et al. [80]. They mounted a silicon heater chip on 1 μm tall SiO_2 spacing pillars on top of an InAs PV cell. The heater was pressed down at the center with a piezo actuator, and a corresponding increase in short-circuit current from the cell was recorded. Since

these initial tests, the same group has reported improvements in their device that enabled higher temperatures, gaps down to 0.12 μm, emitter areas up to 4 cm^2, and reduced heat conduction through the spacers [81]. Hanamura and Mori also demonstrated improved TPV performance due to near-field effects [82]. They used a 16 mm^2 Tungsten emitter held above a GaSb PV cell by a goniometer, which was used to maneuver the emitter to be parallel to the PV cell. The emitter was heated by a constant-power CO_2 laser, and the gap was slowly reduced while measuring temperatures and electrical performance. Below 3 μm, they observed a sharp drop in emitter temperature, consistent with an increase in thermal radiation due to near-field effects. As the gap continued to decrease, output power rose despite a continued drop in emitter temperature, which indicates improved performance as gap size is reduced.

With recent improvements in measuring large-area near-field heat transfer (see Section 2.1), more experimental progress in near-field TPV devices should be realized soon. As better nanofabrication techniques further enable researchers to make these devices, high-performance near-field TPVs may soon be demonstrated. Many improvements to the emitter and absorber have been proposed that should be experimentally investigated, but additional work is also needed to realistically model these alterations considering all losses and especially thermal losses. Thermal losses and temperature dependent effects are often not considered, but these have been shown to be very important to device performance.

3.3 Thermoradiative cells

Unlike a PV or TPV device, a TR cell is the hot object in a heat engine, and it generates power by emitting thermal radiation to colder surroundings. The general class of this type of device, emissive energy harvesters, was proposed by Byrnes et al. in 2014 [85]. Instead of a semiconductor p-n junction, they suggested the use of an infrared rectifying antenna that would capture energy from the emission of the earth to the coldness of outer space. In 2015 Strandberg applied this concept to a semiconductor p-n device in the far-field, introducing TR cells as emissive energy harvesters [6]. The concept of far-field TR cells was also demonstrated experimentally the next year by Santhanam and Fan [86]. In these preliminary works, the working principles of ideal thermoradiative cells were presented, and it was shown that their efficiency can approach the Carnot limit for large bandgap materials. An important characteristic of TR cells was also realized: they have maximum efficiency and maximum power density at different operating voltages [6]. This means that there is an inherent trade-off between these two performance metrics, and the best operating condition is not obvious.

Hsu et al. [87] performed an entropy analysis to demonstrate that TR efficiency may be improved if the cell selectively emits only low-frequency photons to its surroundings. Figure 8 shows the results of their analysis for a thin-film InSb TR cell at 500 K and environment at 300 K. The black line indicates the far-field performance when the InSb cell emits to a blackbody environment, and the red line shows the performance when the environment is replaced with a fictitious selective surface that has narrowband emission/absorption at low frequencies just above the bandgap [87]. The efficiency of the system is improved in this case, because photons with a low frequency have a greater entropy content than photons with a high frequency, making them better carriers for heat rejection as discussed in Section 2.3. However, far-field selective emission will also reduce the power density of the device as a consequence of reduced total emission, also shown in Fig. 8. Utilizing near-field radiation can circumvent this restriction by greatly enhancing the energy transfer as discussed in Section 2.1. When the same TR cell is operated at nanoscale distances and the environment is replaced by $CaCO_3$, shown by the blue lines in Fig. 8, near-field surface phonon polariton modes couple between the InSb cell and the cold $CaCO_3$ receiver. The power density is greatly enhanced while maintaining high efficiencies. If the gap is reduced to 10 nm, the power density can reach values as high as 70 mW/cm^2 with efficiencies remaining above 10% for this idealized case [87]. Figure 8 also shows

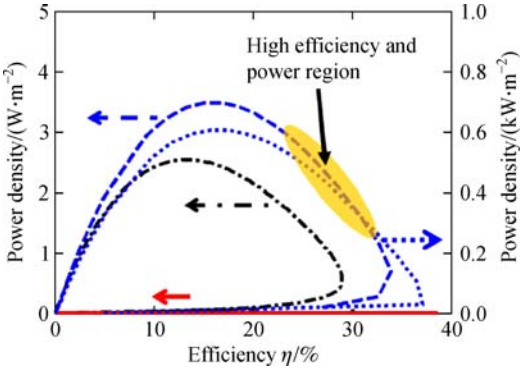

Fig. 8 Thermoradiative device tradeoff between efficiency and power density for a thin-film InSb cell at 500 K emitting to an environment at 300 K. The black dash-dot line indicates far-field radiation between the InSb cell and a blackbody environment. The solid red line shows the far-field performance when the environment is replaced by a fictitious narrowband selective emitter/absorber for low frequencies just above the bandgap. The blue dashed line is for near-field operation with a gap distance of 100 nm and a $CaCO_3$ receiver, and the blue dotted line plotted on the right *y*-axis is for near-field operation with a gap distance of 10 nm and a $CaCO_3$ receiver. In the far-field, use of a selective receiver increases efficiency due to the higher entropy content of low-frequency photons, but it decreases power density due to reduced total radiation exchange. Operating the device in the near-field regime and choosing a receiver that couples to the cell with surface phonon polariton modes increase the power density substantially while maintaining high efficiencies. (Reprinted figure from Hsu et al. [87], under Creative Commons CC-BY license.)

how TR cells have a tradeoff between efficiency and power density, as discussed previously.

Since TR RTECs are so new, very limited additional work has been done to understand and predict their performance with optimized radiation exchange or with losses taken into account. It has been shown that a nanograting on the heat sink could shift the near-field heat transfer to the bandgap frequency and improve performance [88], analogous to what has been proposed for near-field TPV cells. Many of the other proposals for radiation exchange optimization in near-field TPV devices could be applied to TR cells in a similar fashion. A preliminary study has analyzed far-field TR devices considering electron and hole transport properties [89] but more investigation is needed to understand the impacts of loss mechanisms. It is expected that sub-bandgap radiation and non-radiative losses such as Auger recombination could degrade performance, so detailed modeling of the interplay between thermal, electrical, and radiative effects is required. Although experimental near-field demonstration of TR devices has not yet been achieved, this is an important next step for the development of these RTECs. Fortunately, the recent progress described in Section 2.1 on measuring near-field radiative heat transfer between large areas bodes well for experimental evidence of near-field enhancements to TR cells.

3.4 Electroluminescent refrigerators

One way to operate a semiconductor p-n junction as a heat pump is to provide it with an external forward bias voltage, causing the material to emit excess photons and cool below ambient temperature as described in Section 3.1. The first prediction of EL refrigeration was by Tuac in 1957 [7], and evidence for this effect was first provided by Dousmanis et al. in 1963 [90]. Dousmanis et al. examined emission spectra from GaAs light-emitting diodes and showed that a significant portion of the emitted photons had higher energy than the applied voltage, meaning that some of that energy had to come from lattice heat and cool the diode. Berdahl [8] later found that these devices could theoretically achieve cooling power densities equal to the blackbody limit in the far-field and that their maximum efficiency can approach the Carnot limit. Despite these predictions several decades ago, experimental demonstration has been very challenging because any nonidealities in the device can cause heat generation that counteracts the refrigeration effect. Models of the far-field operation of these devices that consider losses such as nonradiative recombination have predicted very low cooling power densities as a result [91–97]. Recently, Santhanam et al. [2] experimentally demonstrated the electroluminescence refrigeration effect for narrow bandgap emitters at high temperature in a low-bias regime. However, the obtained power was extremely low. A review and overview of EL RTEC operation in the far-field can be found in Ref. [98].

Because modeled cooling power densities are quite low for EL devices, there are clear benefits to near-field operation where the radiative transport can be greatly enhanced and the exchange can be quasi-monochromatic if surface modes are leveraged. Chen et al. [99] first investigated near-field effects for EL refrigeration in 2015. They considered an EL device consisting of an InAs diode radiating to a short-circuited diode (surroundings) made of either InAs or InSb, and they considered the effects of Auger recombination and sub-bandgap radiation by surface modes. Auger recombination induces a parasitic heating in the EL refrigerator as the voltage increases, which leads to an optimum operating voltage to achieve maximum cooling power. The materials selected for this study have surface phonon polariton resonant frequencies below the bandgap, so heat transfer due to near-field surface modes is parasitic in nature. When InAs is used for both the EL refrigerator and the hotter receiver, these resonances match and no cooling is achieved. When InSb is used for the receiver, the resonances do not match, which suppresses sub-bandgap radiation exchange by surface mode coupling, and cooling can then be achieved. Even with the losses considered, Chen et al. predict that cooling power densities up to nearly 10 mW/cm^2 and COPs up to 1.65 can be achieved for an InAs EL refrigerator and an InSb receiver with a judicious choice of the gap spacing [99].

More recently, Liu and Zhang [100] developed a multilayer model of a GaSb diode EL refrigerator radiating to a Ge receiver considering sub-bandgap parasitic radiative heat transfer as well as Auger recombination. The considered structure design is schematically illustrated in Fig. 9(a). The forward-biased p-i-n junction is fixed at 290 K with a top Ag strip acting as the anode and bottom Ag substrate acting as the cathode. The hotter receiver is mounted on an Ag substrate and is fixed at 300 K. For a varying vacuum gap spacing d, the maximum refrigeration rate is obtained by optimizing the supplied voltage, and the result is plotted in Fig. 9(b). In this study, GaSb and Ge were purposefully selected because their low-frequency optical properties are not well-matched in order to suppress detrimental sub-bandgap phonon-polariton heat transfer. This leads to higher cooling power densities up to 1 W/cm^2 for a 10 nm gap spacing. Although some parasitic sub-bandgap near-field heat flux still increases as the gap spacing is reduced, the positive effects of increased photon tunneling above the bandgap significantly outweigh this. At large separation distances, the refrigeraton rate approaches the far-field value, and at intermediate distances interference effects cause the refrigeraton rate to exhibit wavy effects with local maxima and minima. Because the parasitic sub-bandgap heat transfer is minimized with this choice of mateirals, the EL refrigerator also becomes much more resistant to non-intrinsic losses, such as Shockley-Read-Hall recombination [100].

These initial models show promising potential for EL

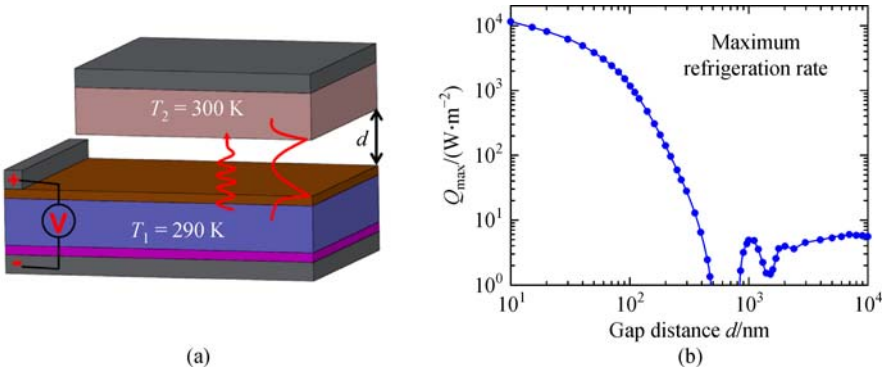

Fig. 9 An electroluminescent refrigerator (a) schematic and (b) maximum refrigeration rate considering Auger recombination and sub-bandgap radiative losses. The p-i-n junction device is GaSb with Ag contacts, and the hotter receiver is Ge mounted on an Ag substrate. The maximum refrigeration rate is obtained by optimizing the operating voltage. At large gap spacing d, the refrigeration rate is a constant at its far-field value where only propagating modes participate in the radiation exchange. At intermediate distances, interference effects cause wavy behavior. Below about half a micron, photon tunneling dominates and the refrigeration rate increases. For these materials, above-bandgap near-field radiation grows more than sub-bandgap phonon polariton parasitic exchange due to the material selection. (Reprinted figure with permission from Elsevier from Liu et al. [100].)

refrigerators operating in the near-field. While far-field devices struggle to achieve positive cooling rates under any nonidealities, the significant enhancement due to near-field radiation can greatly improve the tolerance of devices to these losses. As with TR cells, many opportunities remain to study other mechanisms of optimizing radiation exchange and other choices of materials. Experimental realization of this effect in the near-field is likely to be realized, but challenges still exist in reducing parasitic losses and utilization of very high quality materials to minimize nonintrinsic thermal losses.

3.5 Negative electroluminescent refrigerators

In 1985, Berdahl [8] recognized that in addition to the previously-known EL effect for forward biased p-n junctions, a reverse biased junction can instead cool its environment through negative electroluminescent refrigeration. He showed that in the far-field their cooling rates are blackbody limited, and their COP can approach the Carnot limit if the materials are ideal. The effect was demonstrated experimentally ten years later by Ashley et al. [101] for reverse-biased InSb and CdHgTe diodes. Far-field NEL research progressed quickly [102], and many applications in infrared optoelectronics other than refrigeration (such as radiation screening, control of photodetectors, and reference radiation sources) were realized [103,104]. The use of this phenomenon in refrigeration, though, has been limited since the power density is restricted by the Stefan-Boltzmann law, and the temperature difference (or apparent temperature difference as described in Section 2.2) between the exchanging objects is not very large.

The application of near-field radiation to NEL refrigerators has only been analyzed very recently by Chen et al. [105]. As with the other RTECs, using near-field radiative exchange with materials that support surface modes would be expected to increase the power densities beyond the far-field blackbody limit. Chen et al. studied a hexagonal boron nitride emitter at 290 K (cooled environment) and a mercury cadmium telluride p-n device at 300 K (heat-accepting refrigerator) in both the far-field and near-field limits. For an ideal p-n diode with only radiative recombination and no sub-bandgap radiation due to free carriers, they show that power density can be increased in the near-field by an order of magnitude and the COP is not strongly affected, as expected. This behavior is shown for different vacuum gaps d in Fig. 10(a). When non-idealities such as Auger recombination and sub-bandgap radiation are considered, though, performance is significantly degraded as shown in Fig. 10(b). Auger recombination occurs in the p-n device, but since this is the body receiving radiation, it does not decrease power density as long as the temperature is held constant. In a practical scenario, it would require that much more heat be rejected from the p-n device. The COP is thus degraded due to Auger recombination since more electrical power must be provided to achieve the same cooling rates. Sub-bandgap radiation requires the device to be operated at a higher voltage in the near-field, because detrimental low-frequency radiation from the p-n device to the cold environment is stronger in this regime. The apparent temperature of the refrigerator must be lowered to compensate, which requires a stronger bias. With these losses considered, power densities up to about 100 mW/cm^2 are predicted with corresponding COPs on the order of 0.01.

Although the work by Chen et al. [104] is an important

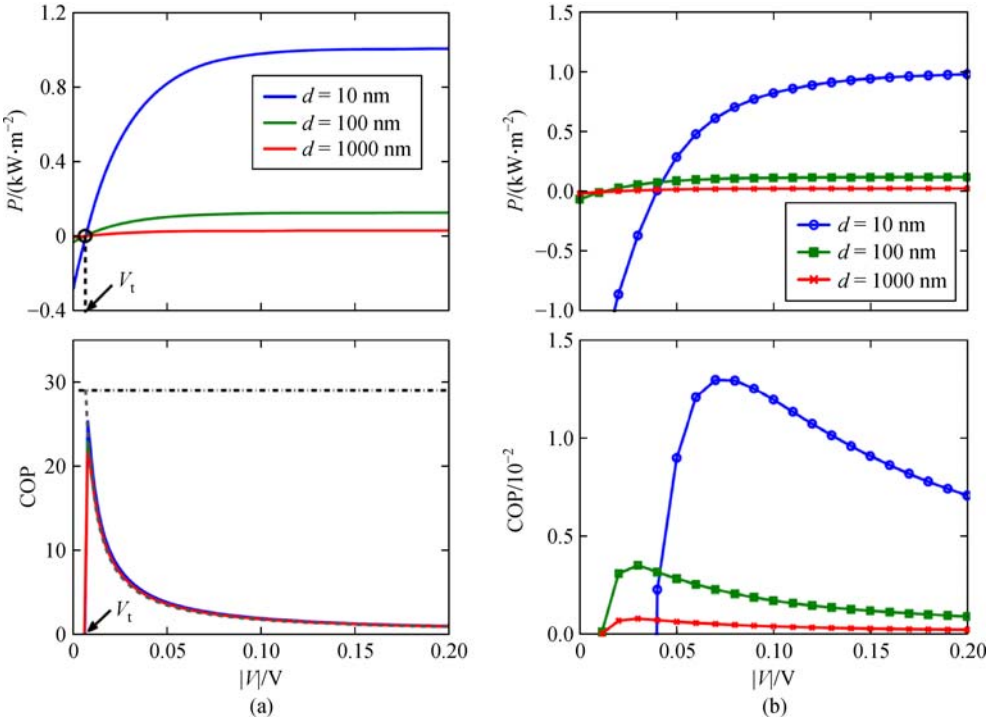

Fig. 10 Power density (P) and coefficient of performance (COP) of a negative electroluminescent refrigerator at 300 K at different vacuum gap distances from the cooled surface at 290 K. (a) represents the ideal case with no Auger recombination and no sub-bandgap radiation due to free carriers, but (b) includes these loss mechanisms. Auger recombination does not decrease power density since it takes place in the p-n device and the temperatures are fixed, but it does degrade the COP. Sub-bandgap free carrier radiation requires the device to be operated at higher voltage in the near-field to make up for increased radiation from the p-n device to the cooled object. (Reprinted with permission from Chen et al. [105]. Copyright 2016 by the American Physical Society)

first step in designing near-field NEL refrigerators, additional modeling work can clarify the impacts of other important effects such as Shockley-Read-Hall recombination, cooling requirements for practical p-n devices, and non-uniform temperature and chemical potential distributions. As suggested for the other RTEC devices, performance could be enhanced by considering alternate material systems or by optimizing the radiative exchange with gratings, graphene layers, or thin films. Since thermal losses occur in the warmer device and these can be mitigated by cooling in an experiment, it is expected that NEL refrigeration may be simpler to demonstrate experimentally than EL refrigeration.

4 Conclusions and outlook

Near-field operation of RTECs offers a path to high power densities and practical applications, although many challenges remain in both the theoretical understanding and experimental demonstration of these devices. Many alterations and improvements have been proposed to optimize radiative exchange in TPV cells; however, comparatively few studies have examined how these perform in the presence of combined electrical, thermal, and radiative losses. The interplay of these loss mechanisms has been shown to significantly affect power output and cooling capabilities. Therefore, it is important to understand how these may vary between different p-n diode materials and different emitters. In particular, reduced surface recombination velocities could enable the enhancements predicted due to quasi-monochromatic near-field heat fluxes associated with surface modes. Because TR, EL, and NEL devices have only recently begun to be analyzed in the near-field, much work remains to determine how near-field radiation may be optimized for each type of RTEC and to determine the impact of different loss mechanisms on individual devices. Due to challenges in measuring large-area near-field radiation exchange, experimental progress lags behind modeling efforts for all RTECs. Near-field performance enhancements have only been demonstrated for TPV cells, and these examples have been fairly limited. Future experimental efforts should focus on verifying increased power density at small vacuum gap spacing as well as examining the various materials and alterations that have been proposed in modeling studies.

Despite these obstacles, there are enormous opportunities for progress, and research in near-field RTECs is poised to rapidly develop. The rich literature and existing

models for TPV cells can be readily applied to TR, EL, and NEL devices. In particular, methods of optimizing radiation exchange for TPVs are expected to function similarly in other RTECs. Alterations such as grating structures proposed for TPVs are already beginning to be mapped to EL refrigerators, and other modifications including backside mirrors, hyperbolic emitters, and graphene layers can similarly be investigated. Additionally, models and understanding of losses in TPV cells are easily applied to other RTECs, since the underlying principles and loss mechanisms are the same. It is clear that these should be considered when predicting device performance, since they have been shown to be crucial in TPVs. Perhaps the most promising area for near-field RTEC progress is experimental demonstrations. Recent developments in measuring large-area near-field radiation and advances in nanofabrication mean that researchers are able to construct devices that were never before possible. It is expected that TR, EL, and NEL devices will soon be demonstrated in the near-field, and this will provide crucial feedback and comparison to modeling efforts. Opportunities also exist in developing high-quality low bandgap semiconductor materials with larger area, fewer defects, and higher temperature tolerances. As the benefits to near-field operation of RTECs are realized, these research efforts may pave the way to a new class of compact, efficient, and useful solid-state heat engines and cooling devices.

Acknowledgements This work was supported by the U.S. Department of Energy, Office of Science, Basic Energy Sciences (Grant No. DE-SC0018369). This material is also based upon work supported by the National Science Foundation Graduate Research Fellowship Program under Grant No. (DGE-1650044). Any opinions, findings, and conclusions or recommendations expressed in this material are those of the authors and do not necessarily reflect the views of the funding agencies.

References

1. Wernsman B, Mahorter R G, Siergiej R, Link S D, Wehrer R J, Belanger S J, Fourspring P, Murray S, Newman F, Taylor D, Rahmlow T. Advanced thermophotovoltaic devices for space nuclear power systems. AIP Conference Proceedings, 2005, 746 (1): 1441–1448
2. Santhanam P, Gray D J, Ram R J. Thermoelectrically pumped light-emitting diodes operating above unity efficiency. Physical Review Letters, 2012, 108(9): 097403
3. Green M A. Solar Cells: Operating Principles, Technology and System Applications. Englewood Cliffs, NJ: Prentice-Hall, Inc., 1982
4. Wedlock B D. Thermo-photo-voltaic energy conversion. Proceedings of the IEEE, 1963, 51(5): 694–698
5. Bauer T. Thermophotovoltaics Basic Principles and Critical Aspects of System Design. Berlin, Heidelberg: Springer-Verlag Berlin Heidelberg, 2011
6. Strandberg R. Theoretical efficiency limits for thermoradiative energy conversion. Journal of Applied Physics, 2015, 117(5): 055105
7. Tauc J. The share of thermal energy taken from the surroundings in the electro-luminescent energy radiated from a p-n junction. Cechoslovackij fiziceskij zurnal, 1957, 7(3): 275–276
8. Berdahl P. Radiant refrigeration by semiconductor diodes. Journal of Applied Physics, 1985, 58(3): 1369–1374
9. Planck M. The Theory of Heat Radiation. Philadelphia, PA: P. Blakiston's Son & Co, 1914
10. Polder D, Van Hove M. Theory of radiative heat transfer between closely spaced bodies. Physical Review B: Condensed Matter and Materials Physics, 1971, 4(10): 3303–3314
11. Pendry J B. Radiative exchange of heat between nanostructures. Journal of Physics Condensed Matter, 1999, 11(35): 6621–6633
12. Joulain K, Mulet J P, Marquier F, Carminati R, Greffet J J. Surface electromagnetic waves thermally excited: radiative heat transfer, coherence properties and Casimir forces revisited in the near field. Surface Science Reports, 2005, 57(3–4): 59–112
13. Basu S, Zhang Z M, Fu C J. Review of near-field thermal radiation and its application to energy conversion. International Journal of Energy Research, 2009, 33(13): 1203–1232
14. Zhang Z M. Nano/microscale Heat Transfer. New York: McGraw-Hill, 2007
15. Biehs S A, Ben-Abdallah P, Rosa F. Nanoscale radiative heat transfer and its applications. In: Morozhenko V, eds. Infrared Radiation. London: InTech, 2012, 1–26
16. Reid M T H, Rodriguez A W, Johnson S G. Fluctuation-induced phenomena in nanoscale systems: harnessing the power of noise. Proceedings of the IEEE, 2013, 101(2): 531–545
17. Song B, Fiorino A, Meyhofer E, Reddy P. Near-field radiative thermal transport: from theory to experiment. AIP Advances, 2015, 5(5): 053503
18. Liu X, Wang L, Zhang Z M. Near-field thermal radiation: recent progress and outlook. Nanoscale and Microscale Thermophysical Engineering, 2015, 19(2): 98–126
19. Francoeur M, Pinar Mengüç M. Role of fluctuational electrodynamics in near-field radiative heat transfer. Journal of Quantitative Spectroscopy & Radiative Transfer, 2008, 109(2): 280–293
20. Hu L, Narayanaswamy A, Chen X, Chen G. Near-field thermal radiation between two closely spaced glass plates exceeding Planck's blackbody radiation law. Applied Physics Letters, 2008, 92(13): 133106
21. Rousseau E, Siria A, Jourdan G, Volz S, Comin F, Chevrier J, Greffet J J. Radiative heat transfer at the nanoscale. Nature Photonics, 2009, 3(9): 514–517
22. St-Gelais R, Guha B, Zhu L, Fan S, Lipson M. Demonstration of strong near-field radiative heat transfer between integrated nanostructures. Nano Letters, 2014, 14(12): 6971–6975
23. Kim K, Song B, Fernández-Hurtado V, Lee W, Jeong W, Cui L, Thompson D, Feist J, Reid M T H, García-Vidal F J, Cuevas J C, Meyhofer E, Reddy P. Radiative heat transfer in the extreme near field. Nature, 2015, 528(7582): 387–391
24. St-Gelais R, Zhu L, Fan S, Lipson M. Near-field radiative heat transfer between parallel structures in the deep subwavelength regime. Nature Nanotechnology, 2016, 11(6): 515–519
25. Shchegrov A V, Joulain K, Carminati R, Greffet J J. Near-field

spectral effects due to electromagnetic surface excitations. Physical Review Letters, 2000, 85(7): 1548–1551
26. Howell J R, Menguc M P, Siegel R. Thermal Radiation Heat Transfer. Boca Raton: CRC press, 2010
27. Rytov S, Kravtsov Y A, Tatarskii V. Priniciples of Statistical Radiophysics: Elements of Random Fields. Berlin: Springer, 1989
28. Francoeur M, Pinar Mengüç M, Vaillon R. Solution of near-field thermal radiation in one-dimensional layered media using dyadic Green's functions and the scattering matrix method. Journal of Quantitative Spectroscopy & Radiative Transfer, 2009, 110(18): 2002–2018
29. Bright T J, Liu X L, Zhang Z M. Energy streamlines in near-field radiative heat transfer between hyperbolic metamaterials. Optics Express, 2014, 22(S4): A1112–A1127
30. Song B, Ganjeh Y, Sadat S, Thompson D, Fiorino A, Fernandez-Hurtado V, Feist J, Garcia-Vidal F J, Cuevas J C, Reddy P, Meyhofer E. Enhancement of near-field radiative heat transfer using polar dielectric thin films. Nature Nanotechnology, 2015, 10 (3): 253–258
31. Shi J W, Liu B A, Li P F, Ng L Y, Shen S. Near-field energy extraction with hyperbolic metamaterials. Nano Letters, 2015, 15 (2): 1217–1221
32. Kim K, Song B, Fernandez-Hurtado V, Lee W, Jeong W H, Cui L J, Thompson D, Feist J, Reid M T H, Garcia-Vidal F J, Cuevas J C, Meyhofer E, Reddy P. Radiative heat transfer in the extreme near field. Nature, 2015, 528(7582): 387–391
33. Ijiro T, Yamada N. Near-field radiative heat transfer between two parallel SiO_2 plates with and without microcavities. Applied Physics Letters, 2015, 106(2): 023103
34. Ito K, Miura A, Iizuka H, Toshiyoshi H. Parallel-plate submicron gap formed by micromachined low-density pillars for near-field radiative heat transfer. Applied Physics Letters, 2015, 106(8): 083504
35. Lim M, Lee S S, Lee B J. Near-field thermal radiation between doped silicon plates at nanoscale gaps. Physical Review B: Condensed Matter and Materials Physics, 2015, 91(19): 195136
36. Bernardi M P, Milovich D, Francoeur M. Radiative heat transfer exceeding the blackbody limit between macroscale planar surfaces separated by a nanosize vacuum gap. Nature Communications, 2016, 7: 12900
37. Watjen J I, Zhao B, Zhang Z M. Near-field radiative heat transfer between doped-Si parallel plates separated by a spacing down to 200 nm. Applied Physics Letters, 2016, 109(20): 203112
38. Boriskina Svetlana V, Tong Jonathan K, Hsu W C, Liao B, Huang Y, Chiloyan V, Chen G. Heat meets light on the nanoscale. Nanophotonics, 2016, 5(1): 134–160
39. Wurfel P. The chemical potential of radiation. Journal of Physics. C. Solid State Physics, 1982, 15(18): 3967–3985
40. Brennan K F. The Physics of Semiconductors. Cambridge: Cambridge University Press, 1999
41. Landsberg P T. Photons at non-zero chemical potential. Journal of Physics. C. Solid State Physics, 1981, 14(32): L1025–L1027
42. Landsberg P T, Tonge G. Thermodynamic energy conversion efficiencies. Journal of Applied Physics, 1980, 51(7): R1–R20
43. Dorofeyev I. Thermodynamic functions of fluctuating electromagnetic fields within a heterogeneous system. Physica Scripta, 2011, 84(5): 055003
44. Essex C, Kennedy D C, Berry R S. How hot is radiation? American Journal of Physics, 2003, 71(10): 969–978
45. Nelson R E. A brief history of thermophotovoltaic development. Semiconductor Science and Technology, 2003, 18(5): S141–S143
46. Broman L. Thermophotovoltaics bibliography. Progress in Photovoltaics: Research and Applications, 1995, 3(1): 65–74
47. Basu S, Chen Y B, Zhang Z M. Microscale radiation in thermophotovoltaic devices—a review. International Journal of Energy Research, 2007, 31(6-7): 689–716
48. Zhou Z G, Sakr E, Sun Y B, Bermel P. Solar thermophotovoltaics: reshaping the solar spectrum. Nanophotonics, 2016, 5(1): 1–21
49. Mustafa K F, Abdullah S, Abdullah M Z, Sopian K. A review of combustion-driven thermoelectric (TE) and thermophotovoltaic (TPV) power systems. Renewable & Sustainable Energy Reviews, 2017, 71: 572–584
50. Datas A, Martí A. Thermophotovoltaic energy in space applications: review and future potential. Solar Energy Materials and Solar Cells, 2017, 161: 285–296
51. Bauer T, Forbes I, Pearsall N. The potential of thermophotovoltaic heat recovery for the UK industry. International Journal of Ambient Energy, 2004, 25(1): 19–25
52. Ostrowski L J, Pernisz U C, Fraas L M. Thermophotovoltaic energy conversion: technology and market potential. AIP Conference Proceedings, 1996, 358(1): 251–262
53. Ungaro C, Gray S K, Gupta M C. Solar thermophotovoltaic system using nanostructures. Optics Express, 2015, 23(19): A1149–A1156
54. Bierman D M, Lenert A, Chan W R, Bhatia B, Celanović I, Soljačić M, Wang E N. Enhanced photovoltaic energy conversion using thermally based spectral shaping. Nature Energy, 2016, 1(6): 16068
55. Wang L P, Zhang Z M. Wavelength-selective and diffuse emitter enhanced by magnetic polaritons for thermophotovoltaics. Applied Physics Letters, 2012, 100(6): 063902
56. Zhao B, Wang L, Shuai Y, Zhang Z M. Thermophotovoltaic emitters based on a two-dimensional grating/thin-film nanostructure. International Journal of Heat and Mass Transfer, 2013, 67: 637–645
57. Tong J K, Hsu W C, Huang Y, Boriskina S V, Chen G. Thin-film 'thermal well' emitters and absorbers for high-efficiency thermophotovoltaics. Scientific Reports, 2015, 5(1): 10661
58. DeSutter J, Bernardi M P, Francoeur M. Determination of thermal emission spectra maximizing thermophotovoltaic performance using a genetic algorithm. Energy Conversion and Management, 2016, 108: 429–438
59. Whale M D. A fluctuational electrodynamic analysis of microscale radiative transfer and the design of microscale thermophotovoltaic devices. Dissertation for the Doctoral Degree. Cambridge, MA: Massachusetts Institute of Technology, 1997
60. Whale M D, Cravalho E G. Modeling and performance of microscale thermophotovoltaic energy conversion devices. IEEE Transactions on Energy Conversion, 2002, 17(1): 130–142
61. Pan J L, Choy H K H, Fonstad C G. Very large radiative transfer over small distances from a black body for thermophotovoltaic applications. IEEE Transactions on Electron Devices, 2000, 47(1):

241–249
62. Narayanaswamy A, Chen G. Surface modes for near field thermophotovoltaics. Applied Physics Letters, 2003, 82(20): 3544–3546
63. Laroche M, Carminati R, Greffet J J. Near-field thermophotovoltaic energy conversion. Journal of Applied Physics, 2006, 100(6): 063704
64. Park K, Basu S, King W P, Zhang Z M. Performance analysis of near-field thermophotovoltaic devices considering absorption distribution. Journal of Quantitative Spectroscopy & Radiative Transfer, 2008, 109(2): 305–316
65. Francoeur M, Vaillon R, Mengüç M P. Thermal impacts on the performance of nanoscale-gap thermophotovoltaic power generators. IEEE Transactions on Energy Conversion, 2011, 26(2): 686–698
66. Ilic O, Jablan M, Joannopoulos J D, Celanovic I, Soljačić M. Overcoming the black body limit in plasmonic and graphene near-field thermophotovoltaic systems. Optics Express, 2012, 20(S3): A366–A384
67. Messina R, Ben-Abdallah P. Graphene-based photovoltaic cells for near-field thermal energy conversion. Scientific Reports, 2013, 3 (1): 1383
68. Guo Y, Jacob Z. Thermal hyperbolic metamaterials. Optics Express, 2013, 21(12): 15014–15019
69. Svetovoy V B, Palasantzas G. Graphene-on-silicon near-field thermophotovoltaic cell. Physical Review Applied, 2014, 2(3): 034006
70. Bright T J, Wang L P, Zhang Z M. Performance of near-field thermophotovoltaic cells enhanced with a backside reflector. Journal of Heat Transfer, 2014, 136(6): 062701–062709
71. Chen K, Santhanam P, Fan S. Suppressing sub-bandgap phonon-polariton heat transfer in near-field thermophotovoltaic devices for waste heat recovery. Applied Physics Letters, 2015, 107(9): 091106
72. Bernardi M P, Dupré O, Blandre E, Chapuis P O, Vaillon R, Francoeur M. Impacts of propagating, frustrated and surface modes on radiative, electrical and thermal losses in nanoscale-gap thermophotovoltaic power generators. Scientific Reports, 2015, 5 (1): 11626
73. Molesky S, Jacob Z. Ideal near-field thermophotovoltaic cells. Physical Review B: Condensed Matter and Materials Physics, 2015, 91(20): 205435
74. Lim M, Jin S, Lee S S, Lee B J. Graphene-assisted Si-InSb thermophotovoltaic system for low temperature applications. Optics Express, 2015, 23(7): A240–A253
75. Chang J Y, Yang Y, Wang L. Tungsten nanowire based hyperbolic metamaterial emitters for near-field thermophotovoltaic applications. International Journal of Heat and Mass Transfer, 2015, 87: 237–247
76. Jin S, Lim M, Lee S S, Lee B J. Hyperbolic metamaterial-based near-field thermophotovoltaic system for hundreds of nanometer vacuum gap. Optics Express, 2016, 24(6): A635–A649
77. Lim M, Lee S S, Lee B J. Effects of multilayered graphene on the performance of near-field thermophotovoltaic system at longer vacuum gap distances. Journal of Quantitative Spectroscopy & Radiative Transfer, 2017, 197: 84–94
78. St-Gelais R, Bhatt G R, Zhu L, Fan S, Lipson M. Hot carrier-based near-field thermophotovoltaic energy conversion. ACS Nano, 2017, 11(3): 3001–3009
79. Watjen J I, Liu X L, Zhao B, Zhang Z M. A computational simulation of using tungsten gratings in near-field thermophotovoltaic devices. Journal of Heat Transfer, 2017, 139(5): 052704
80. DiMatteo R S, Greiff P, Finberg S L, Young-Waithe K A, Choy H K H, Masaki M M, Fonstad C G. Enhanced photogeneration of carriers in a semiconductor via coupling across a nonisothermal nanoscale vacuum gap. Applied Physics Letters, 2001, 79(12): 1894–1896
81. DiMatteo R, Greiff P, Seltzer D, Meulenberg D, Brown E, Carlen E, Kaiser K, Finberg S, Nguyen H, Azarkevich J, Baldasaro P, Beausang J, Danielson L, Dashiell M, DePoy D, Ehsani H, Topper W, Rahner K, Sieriej R. Micron-gap thermophotovoltaics (MTPV). AIP Conference Proceedings, 2004, 738(1): 42–51
82. Hanamura K, Mori K. Nano-gap TPV generation of electricity through evanescent wave in near-field above emitter surface. AIP Conference Proceedings, 2007, 890(1): 291–296
83. Poddubny A, Iorsh I, Belov P, Kivshar Y. Hyperbolic metamaterials. Nature Photonics, 2013, 7(12): 948–957
84. Guo Y, Cortes C L, Molesky S, Jacob Z. Broadband super-Planckian thermal emission from hyperbolic metamaterials. Applied Physics Letters, 2012, 101(13): 131106
85. Byrnes S J, Blanchard R, Capasso F. Harvesting renewable energy from Earth's mid-infrared emissions. Proceedings of the National Academy of Sciences of the United States of America, 2014, 111 (11): 3927–3932
86. Santhanam P, Fan S H. Thermal-to-electrical energy conversion by diodes under negative illumination. Physical Review B: Condensed Matter and Materials Physics, 2016, 93(16): 161410 (R)
87. Hsu W C, Tong J K, Liao B L, Huang Y, Boriskina S V, Chen G. Entropic and near-field improvements of thermoradiative cells. Scientific Reports, 2016, 6(1): 34837
88. Wang B, Lin C, Teo K H, Zhang Z. Thermoradiative device enhanced by near-field coupled structures. Journal of Quantitative Spectroscopy & Radiative Transfer, 2017, 196: 10–16
89. Fernández J J. Thermoradiative energy conversion with quasi-fermi level variations. IEEE Transactions on Electron Devices, 2017, 64(1): 250–255
90. Dousmanis G C, Mueller C W, Nelson H, Petzinger K G. Evidence of refrigerating action by means of photon emission in semiconductor diodes. Physical Review, 1964, 133(1A): A316–A318
91. Mal'Shukov A, Chao K. Opto-thermionic refrigeration in semiconductor heterostructures. Physical Review Letters, 2001, 86(24): 5570–5573
92. Han P, Jin K, Zhou Y, Wang X, Ma Z, Ren S F, Mal'Shukov A G, Chao K A. Analysis of optothermionic refrigeration based on semiconductor heterojunction. Journal of Applied Physics, 2006, 99(7): 074504
93. Yu S Q, Wang J B, Ding D, Johnson S R, Vasileska D, Zhang Y H. Impact of electronic density of states on electroluminescence refrigeration. Solid-State Electronics, 2007, 51(10): 1387–1390
94. Heikkilä O, Oksanen J, Tulkki J. Ultimate limit and temperature dependency of light-emitting diode efficiency. Journal of Applied

Physics, 2009, 105(9): 093119
95. Yen S T, Lee K C. Analysis of heterostructures for electroluminescent refrigeration and light emitting without heat generation. Journal of Applied Physics, 2010, 107(5): 054513
96. Oksanen J, Tulkki J. Thermophotonic heat pump—a theoretical model and numerical simulations. Journal of Applied Physics, 2010, 107(9): 093106
97. Lee K C, Yen S T. Photon recycling effect on electroluminescent refrigeration. Journal of Applied Physics, 2012, 111(1): 014511
98. Santhanam P, Huang D, Gray D J, Ram R J. Electro-luminescent cooling: light emitting diodes above unity efficiency. In: Laser Refrigeration of Solids VI, San Francisco, CA: SPIE, 2013, 863807
99. Chen K, Santhanam P, Sandhu S, Zhu L, Fan S. Heat-flux control and solid-state cooling by regulating chemical potential of photons in near-field electromagnetic heat transfer. Physical Review B: Condensed Matter and Materials Physics, 2015, 91(13): 134301
100. Liu X L, Zhang Z M. High-performance electroluminescent refrigeration enabled by photon tunneling. Nano Energy, 2016, 26: 353–359
101. Ashley T, Elliott C T, Gordon N T, Hall R S, Johnson A D, Pryce G J. Negative luminescence from $In_{1-x}Al_xSb$ and $Cd_xHg_{1-x}Te$ diodes. Infrared Physics & Technology, 1995, 36(7): 1037–1044
102. Elliott C T. Negative luminescence and its applications. Philosophical Transactions of the Royal Society of London Series A: Mathematical, Physical and Engineering Sciences, 2001, 359 (1780): 567
103. Ashley T, Nash G R. Negative luminescence. In: Krier A, eds. Mid-infrared Semiconductor Optoelectronics. London: Springer London, 2006, 453–485
104. Ivanov-Omskii V I, Matveev B A. Negative luminescence and devices based on this phenomenon. Semiconductors, 2007, 41(3): 247–258
105. Chen K, Santhanam P, Fan S. Near-field enhanced negative luminescent refrigeration. Physical Review Applied, 2016, 6(2): 024014